PHYSICAL REVIEW APPLIED **19,** 044076 (2023)

Experimental Implementation of Short-Path Nonadiabatic Geometric Gates in a Superconducting Circuit

Xin-Xin Yang,[1,2] Liang-Liang Guo,[1,2] Hai-Feng Zhang,[1,2] Lei Du,[1,2] Chi Zhang,[1,2] Hao-Ran Tao,[1,2] Yong Chen,[1,2] Peng Duan,[1,2] Zhi-Long Jia,[1,2] Wei-Cheng Kong,[3] and Guo-Ping Guo[1,2,3,*]

[1] *CAS Key Laboratory of Quantum Information, University of Science and Technology of China, Hefei, Anhui 230026, China*

[2] *CAS Center for Excellence in Quantum Information and Quantum Physics, University of Science and Technology of China, Hefei, Anhui 230026, China*

[3] *Origin Quantum Computing Company Limited, Hefei, Anhui 230088, China*

(Received 20 May 2022; revised 16 February 2023; accepted 21 March 2023; published 25 April 2023)

Nonadiabatic geometric quantum computation (NGQC) has attracted a lot of attention for noise-resilient quantum control. However, previous implementations of NGQC require long evolution paths that make them more vulnerable to incoherent errors than their dynamical counterparts. In this work, we experimentally realize a universal short-path nonadiabatic geometric gate set (SP NGQC) with a 2-times shorter evolution path on a superconducting quantum processor. Characterizing with both quantum process tomography and randomized benchmarking methods, we report an average single-qubit gate fidelity of 99.86% and a two-qubit gate fidelity of 97.9%. Additionally, we demonstrate superior robustness of single-qubit SP NGQC gate to Rabi frequency error in some certain parameter space by comparing their performance to those of the dynamical gates and the former NGQC gates.

DOI: 10.1103/PhysRevApplied.19.044076

Quantum computation now is entering the “noisy intermediate-scale quantum” (NISQ) technology era [1], with the fact that quantum processors are susceptible to environmental fluctuations and operational imperfections. To realize quantum logic surpassing the fault-tolerance threshold for large-scale quantum computation [2–4], a universal set of quantum gates, including arbitrary single-qubit gates and a nontrivial two-qubit gate [5,6], is in great request with not only high gate fidelity but also robustness to ambient noise.

Recently, close attention is paid to the geometric phase due to its intrinsic noise-resilience features [7–10]. Unlike the dynamical phase that comes from the time integral of energy, the geometric phase depends only on the evolution path and is immune to any deviation that does not change the enclosed area by the path, which suggests it is noise resilient to certain types of errors [11–18]. With adiabatic cyclic evolutions, geometric [19,20] and holonomic [21–26] quantum gates using the pure geometric phases were demonstrated in physical systems. However, the long run time required by the adiabatic evolution makes quantum gates vulnerable to considerable environment-induced decoherence. Although some transitionless quantum driving algorithms have been put forward to speed up the adiabatic loops, an almost adiabatic process will also introduce unwanted control errors [27–34].

To overcome these drawbacks, nonadiabatic holonomic quantum computation (NHQC) based on the non-Abelian geometric phase [10,35–50], and further the nonadiabatic geometric quantum computation (NGQC) based on the Abelian geometric phase were demonstrated [9,51–53]. For the implementations of NHQC in superconducting transmon qubits [37–40], they involve the lowest three energy levels. However, the relatively short coherence time and the small anharmonicity of the transmon qubits cause extra decoherence and leakage errors [54,55].

In contrast, for NGQC, the nonadiabatic Abelian geometric phases are generated by the cyclic evolution of quantum states with the removal of the dynamic phase. In other words, NGQC involves only two-level computational space with commonly used manipulations and retains the merits of robustness to noises. Lately, NGQC with a so-called orange-slice-shaped evolution path [labeled as NGQC in Fig. 1(b)] is demonstrated in superconducting circuits [52,53]. However, such a long evolution path is time wasting and exposes the qubit to more decoherent errors. To resolve this problem, some modified NGQC schemes such as noncyclic evolutions [56–59] or optimized evolution paths [60–63] have been put forward with shorter evolution paths. Nevertheless, these proposals require careful design and precise parameter control of

---

[*] gpguo@ustc.edu.cn

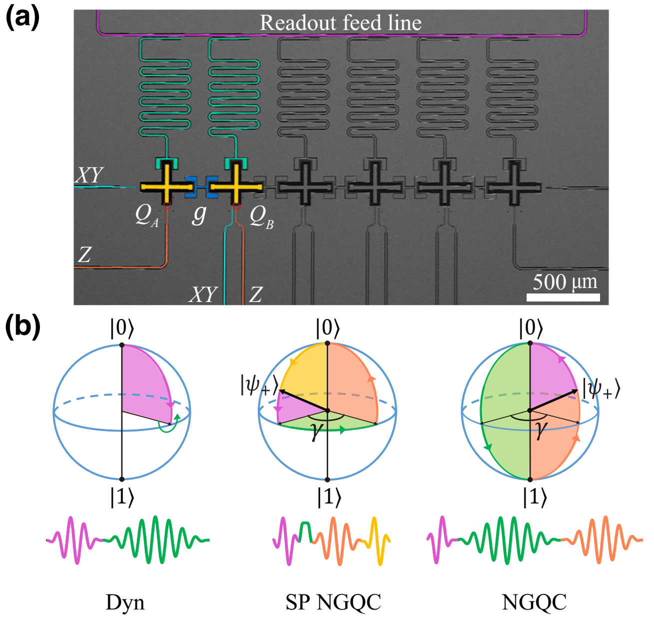

FIG. 1. (a) Electron microscope image of the six-qubit quantum processor. The first two capacitive-coupled qubits, Q_A and Q_B (false colored), are used in this work. (b) Bloch-sphere representations of the evolutionary trajectories to realize single-qubit dynamical and geometric gates and example pulse shapes for Hadamard gate. The dynamical Hadamard gate is implemented with a dynamical $Y/2$ rotation followed by a dynamical X rotation.

the system's Hamiltonian, which makes the experimental realization of short-path NGQC gates more challenging.

Here, we experimentally demonstrate a short-path scheme of NGQC (SP NGQC) in a couple-fixed superconducting chip with a half-orange-slice-shaped evolution loop [labeled as SP NGQC in Fig. 1(b)] that still satisfies the cyclic evolution and parallel transport conditions [64]. Simple and controllable all-microwave manipulations are used to realize the universal geometric quantum gates so that there is no need to consider the versatile pulse distortions. In our experiment, we demonstrate some specific single-qubit nonadiabatic geometric gates with an average fidelity of 99.86(1)% and the two-qubit nonadiabatic CZ gate with a fidelity of 97.9(3)%, which shows a convincing path to reliable and robust universal geometric quantum computation. Furthermore, we also investigate the noise-resilient feature of our short-path geometric gates in contrast with dynamical gates and previous orange-slice-shaped NGQC gates. Particularly, our scheme shows better performance to Rabi frequency error when the rotation angle is large or the rotating axis is close to the z axis.

Before specifying the experimental details, we first give an outline of constructing single-qubit SP NGQC gates. Conventionally, we consider a general setup that a two-level qubit is driven by a classical microwave field. Hereafter, $\hbar$ is set equal to 1. In the interaction picture, the Hamiltonian under the rotating-wave approximations gets

$$H(t)=\frac{1}{2}\begin{pmatrix}\Delta(t) & \Omega(t)\,e^{-i\varphi(t)}\\ \Omega(t)\,e^{i\varphi(t)} & -\Delta(t)\end{pmatrix}, \tag{1}$$

where $\Delta(t)=\omega_q-\omega(t)$ is the frequency difference between the drive $\omega(t)$ and the qubit ω_q, $\Omega(t)$ is called the Rabi frequency, which can be tuned by driving amplitude and $\varphi(t)$ is the phase of the drive. To realize a nonadiabatic single-qubit gate set through a short single evolution loop, we divide the evolution period T into four intervals. In each interval, the microwave field has different amplitude and phases as follows to satisfy the cyclic evolution condition:

$$\int_0^{\tau_1}\Omega(t)\,dt=\frac{\pi}{2}-\theta,\quad \Delta(t)=0,$$
$$\varphi=\phi+\frac{\pi}{2},\quad t\in[0,\tau_1), \tag{2a}$$
$$\Omega(t)=0,\quad \int_{\tau_1}^{\tau_2}\Delta(t)\,dt=\gamma,$$
$$\varphi=\phi+\gamma-\frac{\pi}{2},\quad t\in[\tau_1,\tau_2), \tag{2b}$$
$$\int_{\tau_2}^{\tau_3}\Omega(t)\,dt=\frac{\pi}{2},\quad \Delta(t)=0,$$
$$\varphi=\phi+\gamma-\frac{\pi}{2},\quad t\in[\tau_2,\tau_3), \tag{2c}$$
$$\int_{\tau_3}^{T}\Omega(t)\,dt=\theta,\quad \Delta(t)=0,$$
$$\varphi=\phi+\frac{\pi}{2},\quad t\in[\tau_3,T]. \tag{2d}$$

The final evolution operator can be obtained as

$$U(T)=\cos\frac{\gamma}{2}-i\sin\frac{\gamma}{2}\begin{pmatrix}\cos\theta & \sin\theta\,e^{-i\phi}\\ \sin\theta\,e^{i\phi} & -\cos\theta\end{pmatrix}$$
$$=e^{-i(\gamma/2)\mathbf{n}\cdot\boldsymbol{\sigma}}. \tag{3}$$

The operator $U(T)$ represents rotation operations around the axis $\mathbf{n}=(\sin\theta\cos\phi,\sin\theta\sin\phi,\cos\theta)$ with an angle γ, where $\boldsymbol{\sigma}=(\sigma_x,\sigma_y,\sigma_z)$ are the Pauli operators. θ, ϕ, γ are determined by the drive. Following the evolution, two orthogonal eigenstates $|\psi_+\rangle=\cos(\theta/2)\,|0\rangle+\sin(\theta/2)\,e^{i\phi}\,|1\rangle$ and $|\psi_-\rangle=\sin(\theta/2)\,e^{-i\phi}\,|0\rangle-\cos(\theta/2)\,|1\rangle$ of $U(T)$ undergo a cyclic half-orange-slice-shaped path with an enclosed solid angle equal to the rotation angle γ [see the Bloch sphere labeled with SP NGQC in Fig. 1(b)], resulting in a geometric phase $-\gamma/2$ ($\gamma/2$) on the quantum state $|\psi_+\rangle$ ($|\psi_-\rangle$). (Detailed calculation can be found in Appendix D.) A comparison of the gate time between the conventional dynamical gate (Dyn), the NGQC gate, and the SP NGQC gate is shown in Fig. 1(b). It can be seen that the SP NGQC gate has a relatively short evolution path and the gate time can be further shortened to twice smaller than the NGQC scheme without the green part by applying virtual Z gates [65].

Our experiment is performed in a six-transmon-qubit-chain device [66]. The two adjacent qubits used in this experiment and their coupling capacitance are shown in Fig. 1(a). Each qubit equips a microwave line for driving, a flux-bias line to tune the frequency, and a $\lambda/4$ resonator for individual and simultaneous readout. The transition frequency of Q_A and Q_B are $\omega_A/2\pi = 5.511$ GHz and $\omega_B/2\pi = 5.001$ GHz, respectively. Moreover, the anharmonicities of the qubit are $\alpha_A/2\pi = -242.6$ MHz and $\alpha_B/2\pi = -250.0$ MHz, respectively, ensuring a well-defined two-level system to encode the qubits. The fixed capacitive-coupling strength $g_{AB}/2\pi$ between two qubits is about 10 MHz. More details about the device parameters and the measuring circuits can be found in Appendix A.

The single-qubit SP NGQC gates are performed on Q_A. To show the ability to construct a universal single-qubit gate set, we implement Hadamard gate (H), π, and $\pi/2$ rotations around both X and Y axes (denoted as X, $X/2$, Y, $Y/2$, respectively). Taking advantage of the virtual Z gate, the geometric gate is a composite of three rotations with a rotation angle no more than $\pi/2$. For simplicity, we fix the single interval's period τ to 20 ns with 5-ns buffer times both before and after it to prevent the microwave reflection. Then the fixed gate length of a geometric gate is 90 ns, and the magnitude of the microwave is tuned to control the rotation angle. The envelope of each pulse is cosine shaped and the derivative removal by adiabatic gate (DRAG) correction is also used to suppress the leakage to the undesired energy levels, especially $|2\rangle$ state [67].

We first use the quantum process tomography (QPT) method to characterize the performance of these single-qubit geometric gates [68–70]. The experimental process matrix χ_{exp} of four specific geometric gates X, $X/2$, $Y/2$, and H are shown in Fig. 2(a) with an average gate fidelity of 99.3(1)%. Considering that the process fidelities contain the state preparation and measurement (SPAM) errors, we then utilize another commonly used method, Clifford-based randomized benchmarking (RB) [70–72], to characterize the geometric gates. The experimentally measured ground-state probability (the sequence fidelity) decays as a function of the number of single-qubit Clifford gates m are shown in Fig. 2(b). The reference RB experiment gives an average gate fidelity 99.86(1)% for the realized single-qubit gates in the Clifford group. The measured interleaved gate fidelities of the four specific gates X, $X/2$, Y, and $Y/2$ are 99.83(2)%, 99.79(2)%, 99.80(2)%, and 99.79(1)%, respectively. All the data are corrected for readout errors and the corresponding readout fidelity matrixes are listed in Appendix C.

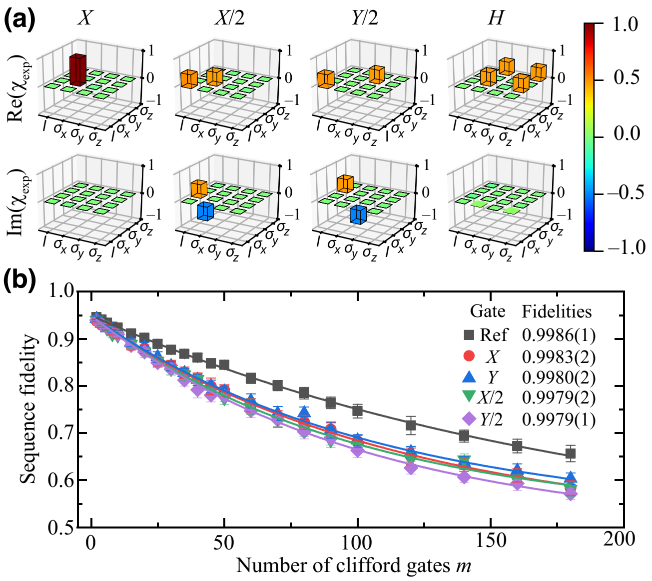

FIG. 2. Characterization of the single-qubit SP NGQC gates. (a) Bar charts of the real and imaginary part of χ_{exp}. Four specific gates—X, $X/2$, $Y/2$, and H—are shown with process fidelities of 99.5(1)%, 99.5(2)%, 98.8(4)%, and 99.0(5)%, respectively. The solid black outlines are χ_{ideal} for the ideal gates. (b) RB of single-qubit SP NGQC gates. Fitting the reference RB and interleaved RB decay curves gives the gate fidelity of four specific gates: X, Y, $X/2$, and $Y/2$.

After demonstrating high-fidelity single-qubit SP NGQC gates, we deliberate on the noise-resilient characteristic of these gates. All noise can be attributed to the effect on the axis of rotation and the angle of rotation. Here, we focus on two typical types of errors: Rabi frequency error through changing the microwave driving amplitude by an amount of δA, and frequency shift error by changing the microwave driving frequency by an amount of $\delta\Delta$. The Rabi frequency error is an intuitive manifestation of rotation angle error and the frequency shift error affects the rotation angle. As shown in Figs. 3(a)–3(d), we compare the performance of both $X/2$ and H gates with three evolution paths, evaluated by the process fidelities from QPT. These figures show that in the case of Rabi frequency error, the geometric gates are more robust than the dynamical gates, and for the H gate, the SP NGQC gate is the most robust one. However, for the frequency shift error, the SP NGQC gates are not as good as the other two types of gates.

To explain the noise-resilient features of different types of gates, we theoretically calculate the fidelity changing with an extra Rabi frequency error term δA. For the frequency shift error $\delta\Delta$, the process fidelity of the gates is not as intuitive as Rabi frequency error to formulate, and theoretical results are obtained using master-equation

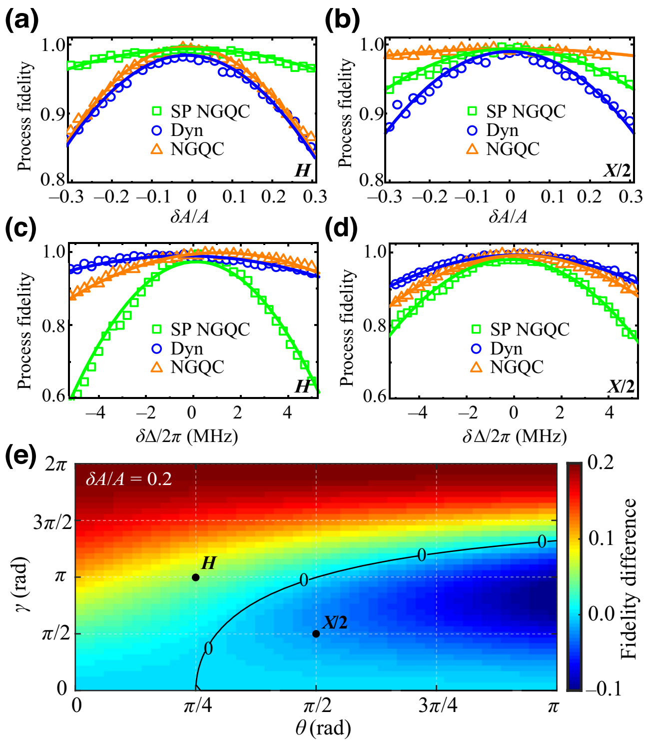

FIG. 3. Noise-resilient feature of SP NGQC single-qubit gates. $X/2$ and H gates are chosen for rotating axes in different planes. (a) and (b) are, respectively, the process fidelities of quantum gates H and $X/2$ as a function of Rabi frequency error δA. (c) and (d) are, respectively, the process fidelities of quantum gates H and $X/2$ as a function of qubit-frequency shift error $\delta\Delta$. Performances of different evolution paths including the dynamic (Dyn), the NGQC, and the SP NGQC are shown for comparison. The experimental results are also consistent with the numerical simulations (solid lines). (e) The landscape of process fidelity difference $F_{\text{SP NGQC}} - F_{\text{NGQC}}$ versus θ and γ where $\delta A/A = 0.2$. Black dots show the working points for (a),(b).

numerical simulation (see the Appendix G for more details). The calculated fidelities are overlaid on Fig. 3, which shows our theoretical formulas agree well with the experimental results. Since the Hamiltonian of SP NGQC has σ_z component, the frequency shift error changes the evolution path of SP NGQC significantly, and our SP NGQC scheme does not perform well under this error compared to the other two schemes. For the reason why our gates perform best for the H gate against the Rabi frequency error, we then calculate the fidelity difference $F_{\text{SP NGQC}} - F_{\text{NGQC}}$ as a function of both θ and γ, which contains the universal single-qubit gates. As shown in Fig. 3(e), where $\delta A/A$ is fixed to 0.2, the SP NGQC gates are better than the traditional NGQC gates when the rotating axis is close to the z axis (θ is small) or the rotation angle γ is large, which reflects the short-path advantage of our SP NGQC gates.

In order to achieve a universal SP NGQC, we also realize the nontrivial two-qubit geometric CZ gate similarly to the single-qubit case. To fully control the rotation angle and coupling strength between $|11\rangle$ and $|20\rangle$ states, we utilize the radiofrequency flux-modulation method without extra z-pulse distortion correction [73,74]. Here, $|AB\rangle$ denotes the state of $|Q_A, Q_B\rangle$. The frequency of Q_A is modulated with a cosinoidal form: $\omega_A(t) = \bar{\omega}_A + \varepsilon\cos(2\nu t + 2\Phi)$, where $\bar{\omega}_A$ is the mean operating frequency, ε, ν, and Φ are the modulation amplitude, frequency, and phase, respectively. The factor of 2 arises because Q_A is at the sweet spot, and the frequency undergoes two cycles for each cycle of flux. Ignoring the higher-order oscillating terms, the obtained effective Hamiltonian in the interacting picture can be reduced to

$$H = \frac{1}{2}\begin{pmatrix} \Delta' & g_{\text{eff}}\, e^{i\beta} \\ g_{\text{eff}}\, e^{-i\beta} & -\Delta' \end{pmatrix} \tag{4}$$

in the subspace $\{|11\rangle, |20\rangle\}$, where $\Delta' = |\bar{\omega}_A - \omega_B| - \alpha_A - 2\nu$ and $\beta = \Phi + \pi/2$. The effective coupling strength g_{eff} is equal to $2\sqrt{2}g_{AB}J_1(\varepsilon/2\nu)$ and $J_1(\varepsilon/2\nu)$ is the first-order Bessel function of the first kind.

Similar to the single-qubit Z rotation described by the Hamiltonian in Eq. (1), we can acquire a pure geometric phase $e^{-i\gamma'/2}$ on the state of $|11\rangle$. Thus, within the computational subspace $|00\rangle, |01\rangle, |10\rangle, |11\rangle$, the resulting unitary operation corresponding to a controlled-phase gate with a geometric phase γ' is

$$U_2(\gamma') = \begin{pmatrix} 1 & 0 & 0 & 0 \\ 0 & 1 & 0 & 0 \\ 0 & 0 & 1 & 0 \\ 0 & 0 & 0 & e^{-i\gamma'/2} \end{pmatrix}. \tag{5}$$

By setting $\gamma' = 2\pi$, we can achieve a CZ gate. According to Eq. (2), a rotation around z axis requires $\theta = 0$ so that the time of the fourth segment corresponding to Eq. (2d) is equal to zero.

Accordingly, the two-qubit geometric CZ gate is performed with three cosinoidal modulation drives applied in series. Each has a flat-topped Gaussian envelope with 20-ns rising and falling edges to suppress the undesired impact of a sudden phase change of the microwave modulation. The modulation frequency $\nu/2\pi = 80$ MHz and the modulation amplitude $\varepsilon/2\pi = 107.8$ MHz lead to an efficient coupling strength $g_{\text{eff}}/2\pi \approx 9$ MHz. We cannot realize zero coupling strength required by Eq. (2b) using parametric driving. But CZ gate is quite special with $\gamma' = 2\pi$, which corresponds to the solid angle of a hemisphere. Therefore, the trajectory on the Bloch sphere formed by any plane passing through the center of the sphere can meet that requirement, and $g_{\text{eff}}/2\pi$ is not restricted to 0 in the second segment. The modulation amplitude is tuned to 100 MHz at the second part causing $\Delta'/2\pi = 7$ MHz. The

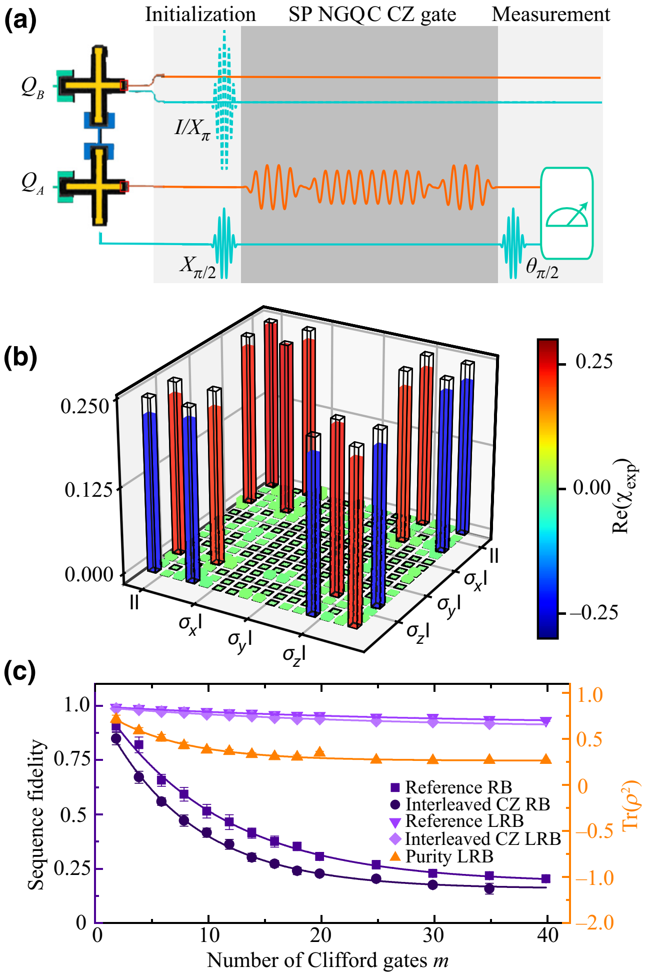

FIG. 4. Two-qubit SP NGQC CZ gate. (a) Experimental pulse sequence to acquire conditional phase of the geometric controlled-phase gate. The conditional phase is the phase difference in Q_A due to Q_B occupying either $|0\rangle$ or $|1\rangle$. (b) The real part of the experimental process matrix χ_{exp} for the geometric CZ gate. The imaginary part is not shown, theoretically all its elements are zero and experimentally they are smaller than 0.02. The solid black outlines are for the ideal CZ gate. The process fidelity is 94.2(2)% after maximum-likelihood estimation [69]. (c) Randomized benchmarking data for the geometric CZ gate. Fitting to both reference and interleaved RB curves gives the gate fidelity 97.9(3)%. Reference and interleaved LRB gives a leakage error of 0.13%. The purity RB (right axis) shows an incoherent error of 3.7%.

experimental sequence we use to acquire the conditional phase is shown in Fig. 4(a). Note that the first and third intervals are resonant operations with trajectories along the geodesic. According to the geodesic rule [75], these operations do not accumulate dynamical phases and thus do not influence the final conditional phase. We first run the experiment with only the first and second segments and sweep the length of the second segment to find the working region where the conditional phase is close to π. Then within that region, we add the third segment and sweep the microwave's phase and time to bring the state back to $|11\rangle$. Consequently, the total effective gate time is 189.375 ns. The detailed evolution path and the conditional phase against pulse times can be seen in Appendix I.

Likewise, we characterize the CZ gate with both QPT and RB methods. For QPT, the experimentally reconstructed process matrix of the CZ gate is shown in Fig. 4(b) and indicates a process fidelity of 94.2(2)%. Besides, we extract the CZ gate fidelity $F_{\text{CZ}} = 97.9(3)\%$ from fitting both the reference and interleaved RB decay curves. To further investigate the error budgets, we first quantitatively extract the particular gate error from the QPT and get the error rates from decoherence (4.3%), dynamic *ZZ* coupling (1.3%), and SPAM (0.3%), respectively, following the error matrix method developed by Korotkov [76]. To examine the leakage error, we perform leakage RB (LRB) [see Fig. 4(c)] and extract a leakage rate $L_1^{\text{CZ}} = 0.13\%$ per CZ gate by fitting the state population in the computational subspace $|00\rangle, |01\rangle, |10\rangle, |11\rangle$ [77,78]. We find that most residual leakage is introduced into the second excited state of Q_A, which indicates it may come from the residual pulse distortion in *Z*-control pulses of Q_A. We then perform purity RB [also see Fig. 4(c)] to check the incoherent error [79]. The purity RB experiment is done by performing QST instead of measuring the state probability at the end of the sequence and gives the incoherent error $\epsilon = 3.7\%$ per CZ gate, which is comparable with the results obtained from QPT. Taken together, the main error in the demonstrated two-qubit SP NGQC CZ gate comes from decoherence in our qubits, which could be further improved by optimizing the device design and fabrication. Another way to improve it is to use a more complicated control optimization scheme (Appendix J). Moreover, a quantum circuit with tunable couplers may also help to suppress these errors by reducing operating time [80,81].

In conclusion, we experimentally realize single-qubit short-path nonadiabatic geometric gates with a 2-times shorter evolution path and fidelities above 99.86(1)%. We illustrate the significant advantages of our gates that are resilient to control amplitude noise, especially when the rotating axis is close to the *z* axis or the rotation angle is large, by comparing the performance with the orange-slice-shaped geometric gates and the dynamical gates. Besides, we also demonstrate the two-qubit nonadiabatic geometric controlled-*Z* gate with all-microwave controls to prevent complicated flux pulse distortion calibrations. The CZ gate has a comparable fidelity of 97.9(3)%, mainly limited by the qubit decoherence time. Consequently, the shown universal geometric quantum gate set paves the way for high-fidelity robust geometric quantum computation for NISQ-era applications. Other experimental systems, such as trapped ions [82] and semiconductor quantum dots [83] can also benefit from the methods utilized here for the geometric realization of universal gates.

ACKNOWLEDGMENTS

We thank Sai Li and Zheng-Yuan Xue for helpful theoretical discussion. We also thank Gang Cao and Hai-Ou Li for helpful discussions and improving the paper. This work is supported by the National Natural Science Foundation of China (Grant No. 12034018), and this work is partially carried out at the USTC Center for Micro and Nanoscale Research and Fabrication.

APPENDIX A: EXPERIMENTAL SETUP

Our experiments are implemented on a six-transmon-qubit-chain device, which consists of six adjacent cross-shaped transmon qubits arranged in a linear array with nearly identical nearest-neighbor coupling strengths $g/2\pi \approx 10$ MHz, as illustrated in Fig. 1(a). The qubits in the device are frequency-tunable transmons, of which the frequencies can be adjusted individually by tuning the external magnetic field through the Z control line and the qubits can be driven through the XY control lines. Each qubit can be read out by the individual $\lambda/4$ resonators, where the resonators are coupled to the transmission line. In the experiments, we perform short-path geometric gates with the first two adjacent qubits Q_A and Q_B, whose main parameters are summarized and listed in Table I. The other four qubits are biased far away from these two operation qubits and thus are nearly completely decoupled. Both qubits work at the sweet spots to maintain the best operating performance.

TABLE I. Device parameters of the two operating qubits.

Parameters	Q_A	Q_B
Readout frequency (GHz)	6.5455	6.4005
Qubit frequency (GHz)	5.5114	5.0010
Anharmonicity ($\alpha/2\pi$) (MHz)	−242.6	−250.0
T_1 (μs) (sweet spot)	11.5	22.3
T_2^* (μs) (sweet spot)	7.5	27.8
T_1 (μs) (CZ working point)	10.6	22.3
T_2^* (μs) (CZ working point)	5.9	27.8
Readout fidelity $\|0\rangle$ (F_0)	97%	96%
Readout fidelity $\|1\rangle$ (F_1)	91%	90%
Readout fidelity $\|2\rangle$ (F_2)	85%	...
Qubit-qubit coupling strength $g_{AB}/2\pi$ (MHz)	9.5	
Qubit-readout dispersive shift χ_{01} (MHz)	0.55	0.3

The sample is cooled down to 10 mK within a dilution refrigerator of Oxford Triton XL. The wiring diagram and circuit components for control and readout of qubits are shown in Fig. 5. In the dilution refrigerator, attenuators and filters are installed at different stages to reduce noise. The qubits are controlled by a highly integrated quantum control system, Quantum AIO from OriginQ Inc. [84]. For qubit-state readout, the readout signal after dual-quadrature up-conversion in Quantum AIO passes through the attenuators and filters and then reaches the quantum

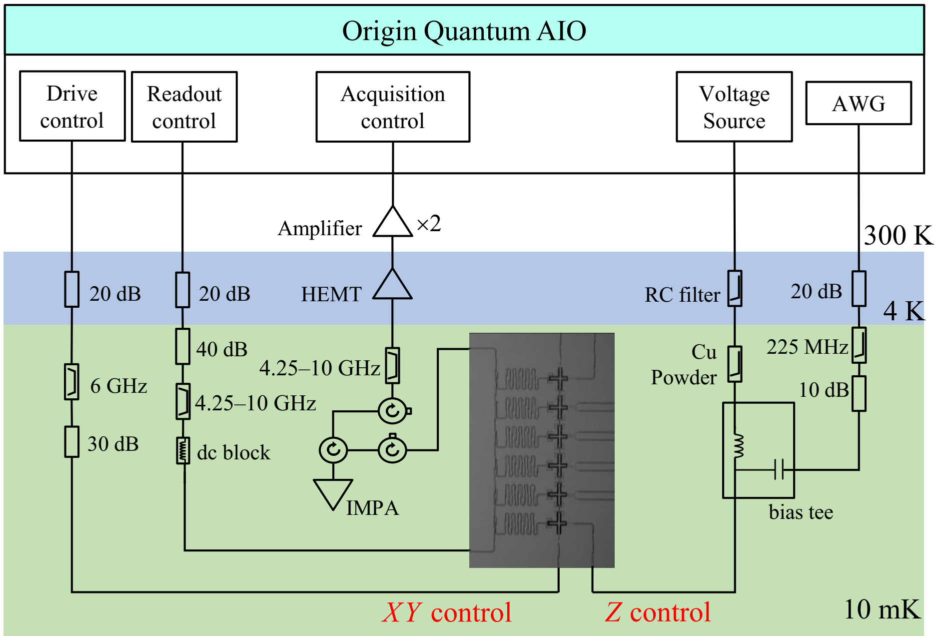

FIG. 5. Details of wiring and circuit component. Testing equipments are supported by a highly integrated quantum computer control system from OriginQ Inc. at room temperature. In the dilution refrigerator, attenuates and filters are installed at different stages to reduce noise. An IMPA and three amplifiers are used to acquire adequate signal-to-noise ratio.

processor. The output signal firstly passes through two circulators, then is amplified by an impedance transformer parametric amplifier (IMPA) [85], of which the noise as well as the noise from higher-temperature stages has been blocked by the preceding of two circulators. The IMPA with an amplification gain of 15 dB and a bandwidth about 500 MHz allows high-fidelity single-shot measurements of the two qubits individually and simultaneously. Being magnified by a high electron mobility transistor (HEMT) amplifier at the 4-K stage and two low-noise amplifiers at room temperature, respectively, the signal is finally captured and analyzed by the Quantum AIO.

APPENDIX B: CROSSTALK

Crosstalk between Z control lines of the two qubits is inevitable due to the ground plane return currents. For dc flux bias to control the working frequency of the qubits, we measure the crosstalk between the Z control lines and qubits to be approximately 10%. The crosstalk can be compensated by orthonormalizing the Z bias lines through an inversion of the normalized qubit frequency response matrix

$$M = \begin{pmatrix} 1.0000 & -0.1001 \\ 0.1546 & 1.0000 \end{pmatrix}. \tag{B1}$$

For parametric driving of qubits, additional calibration of the phase difference between two control lines of qubits is needed. The experimental sequence to measure the phase difference is shown in Fig. 6 and the phase difference of the Z control lines of Q_B with respect to Q_A is 3.3681 rad at an 80-MHz parametric driving frequency. The driving frequency will influence the phase difference and slightly change the qubit frequency response matrix, as

$$M = \begin{pmatrix} 1.0000 & -0.0974 \\ -0.1572 & 1.0000 \end{pmatrix} \tag{B2}$$

at 80 MHz.

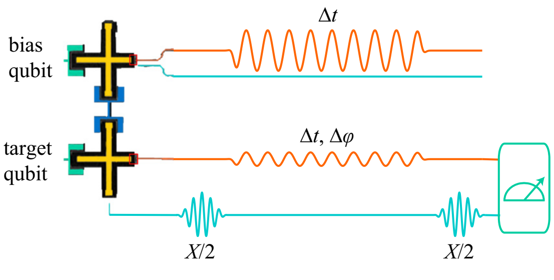

FIG. 6. Experimental pulse sequence to measure the phase difference between the two-qubit Z control lines. For each $\Delta\varphi$, we sweep Δt to acquire the frequency of the target qubit under the parametric control. The frequency of the target qubit reaches a modulational maximum when $\Delta\varphi$ is tuned synchronous with the bias qubit.

APPENDIX C: READOUT CALIBRATION

Due to the thermal fluctuations and qubit relaxation during measurements, there are non-negligible readout infidelities. The intrinsic probabilities for the single qubit can be inferred from the measured probabilities $P_M = (P_0, P_1)^T$ and the measurement fidelities are gotten by preparing the system in each computational basis state and simultaneously measuring the assignment probability of the qubit for 10 000 executions (Table I). The intrinsic occupation probabilities are computed as $P_i = F^{-1} \cdot P_M$ where

$$F = \begin{pmatrix} F_0 & 1-F_1 \\ 1-F_0 & F_1 \end{pmatrix}. \tag{C1}$$

For two qubits, the readout fidelity matrix is then given by $F_{Q_A} \otimes F_{Q_B}$. However, we need to read and calibrate the second excited state of the qubit in leakage RB so the fidelity matrix should be expanded to 3×3 dimensions. On account of poor control of the $|2\rangle$ state of Q_B, we prepare and simultaneously measure the assignment probability $P_M = (P_{00}, P_{01}, P_{10}, P_{11}, P_{20}, P_{21})^T$ of the two qubits, and take the sum probability of state $|20\rangle$ and $|21\rangle$ as leakage. The measured two-qubit readout fidelity matrix is shown as

$$\begin{array}{c|cccccc|} & |00\rangle & |01\rangle & |10\rangle & |11\rangle & |20\rangle & |21\rangle \\ \langle 00| & 0.912 & 0.085 & 0.088 & 0.008 & 0.035 & 0.005 \\ \langle 01| & 0.059 & 0.888 & 0.005 & 0.085 & 0.002 & 0.049 \\ \langle 10| & 0.026 & 0.002 & 0.834 & 0.077 & 0.107 & 0.008 \\ \langle 11| & 0.001 & 0.023 & 0.057 & 0.812 & 0.004 & 0.023 \\ \langle 20| & 0.001 & 0.000 & 0.013 & 0.003 & 0.819 & 0.145 \\ \langle 21| & 0.000 & 0.002 & 0.001 & 0.014 & 0.031 & 0.769 \end{array}. \tag{C2}$$

APPENDIX D: THE GEOMETRY OF SP NGQC

Nonadiabatic Abelian geometric phases are generated by the cyclic evolution and parallel transport of a state subspace in the Hilbert space. Following the evolution path described by Eq. (2), the two orthogonal bases $|\psi_+\rangle$ and $|\psi_-\rangle$ can undergo cyclic evolution,

$$|\psi_+\rangle \rightarrow U(T)\,|\psi_+\rangle = e^{-i\gamma/2}\,|\psi_+\rangle\,, \tag{D1}$$

$$|\psi_-\rangle \rightarrow U(T)\,|\psi_-\rangle = e^{i\gamma/2}\,|\psi_+\rangle\,, \tag{D2}$$

and they, respectively, acquire phases $-\gamma/2$ and $\gamma/2$. Driven by the designed Hamiltonian, the two orthogonal bases can evolve along the geodesic on the Bloch sphere. Similar to the parallel transport of a vector, no dynamical phase is accumulated for the state moving along the geodesic lines. Quantitatively, the dynamical phase γ_d accumulated during the evolution path is calculated by

$$\gamma_d = \int_\tau \langle\psi_\pm(t)|\, H(t)\, |\psi_\pm(t)\rangle\, dt = 0 \tag{D3}$$

for each segment of the evolution path, where $|\psi_\pm(t)\rangle = U(t)\,|\psi_\pm\rangle$ with $U(t)$ being the evolution operator and $H(t)$ is Eq. (1) in the main text. Therefore, only geometric phases $-\gamma/2$ and $\gamma/2$ are accumulated in the process. Using the Bloch-sphere representation for the evolution of the basis $|\psi_+\rangle$, γ is proportional to the solid angle enclosed by the half-orange-slice-shaped loop, shown in Fig. 1(b). This corresponds to an essential feature of nonadiabatic Abelian geometric phases, i.e., the geometric phase is equal to half of the solid angle subtended by a curve traced on a sphere [9].

APPENDIX E: NGQC WITH ORANGE-SLICE LOOPS

We present the details in implementing previous NGQC with orange-slice-shaped loops [52,53]. The evolution path is divided into three intervals with resonant drive, which has different amplitudes and phases satisfying

$$\int_0^{\tau_1} \Omega(t)\, dt = \theta, \quad \varphi = \phi - \frac{\pi}{2}, \quad t \in [0, \tau_1), \tag{E1a}$$

$$\int_{\tau_1}^{\tau_2} \Omega(t)\, dt = \pi, \quad \varphi = \phi + \gamma + \frac{\pi}{2}, \quad t \in [\tau_1, \tau_2), \tag{E1b}$$

$$\int_{\tau_2}^{T} \Omega(t)\, dt = \pi - \theta, \quad \varphi = \phi - \frac{\pi}{2}, \quad t \in [\tau_2, T]. \tag{E1c}$$

The final evolution operator can be obtained as $U(T) = e^{i\gamma \mathbf{n}\cdot\boldsymbol{\sigma}}$, which corresponds to a rotation operation around the axis $\mathbf{n}$ by an angle -2γ.

The performance of single-qubit gates and its gate robustness against amplitude error is shown in Figs. 3(a) and 3(b). And the same-loop two-qubit CZ gate has the fidelity of 98.1(1)% using the RB method (shown in Fig. 7). The fidelity is slightly higher than the short-path CZ gate because the effective gate length of the orange-slice-shaped CZ gate is 85 ns, which suffers less incoherent errors.

APPENDIX F: QUANTUM PROCESS TOMOGRAPHY

Quantum process tomography is used to characterize both the single-qubit and two-qubit gates [68–70]. For N-qubit gate, we first prepare a set of initial states $\{|0\rangle, |1\rangle, (|0\rangle - i|1\rangle)/\sqrt{2}, (|0\rangle + |1\rangle)/\sqrt{2}\}^{\otimes N}$, and measure with standard quantum state tomography (QST) with

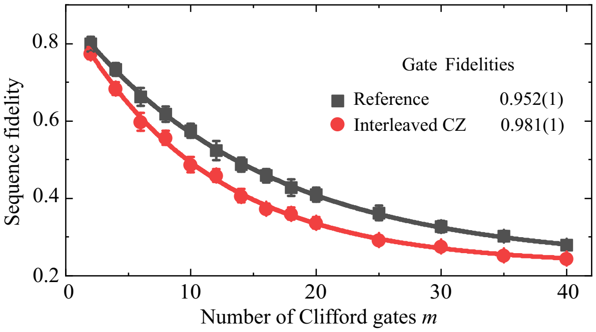

FIG. 7. Reference and interleaved RB results for the two-qubit NGQC CZ gate. Fitting to both reference and interleaved RB curves gives the gate fidelity 98.1(1)%.

prerotations $\{I, X/2, Y/2\}^{\otimes N}$ to get the density matrix $\{\rho_i\}$ of input states. Then a specific nonadiabatic geometric gate is applied following the initial states' preparation. Finally, we measure the output states with QST and reconstruct the output states $\{\rho_f\}$. By mapping between the input states and output states, we can determine the process matrix χ_{exp} of the geometric gate through $\rho_f = \sum_{\text{m,n}} \chi_{\text{mn}} E_m \rho_i E_n^\dagger$, where the basis operators E_m and E_n are chosen from the set $\{I, \sigma_x, \sigma_y, \sigma_z\}^{\otimes N}$ with σ_x, σ_y, and σ_z being Pauli operators.

Based on the fact that the experiments are disturbed by various noises such as coherent errors due to imperfect control, decoherence error, state preparation and measurement error, and so on, the experimental process matrix χ_{exp} is different with the corresponding ideal process matrix χ_{ideal} and the difference is evaluated by the process fidelity $F_p = \text{Tr}(\chi_{\text{exp}}\chi_{\text{ideal}})$. Each QPT experiment for the specific gate is repeated 4 times for the sake of eliminating the measurement uncertainty. The error analysis in QPT is obtained from bootstrap resampling.

For the two-qubit gates, we follow a method developed by Korotkov [76] to further distinguish the error sources. First, we extract the SPAM error by comparing the experimentally reconstructed input states $\{\rho_i\}$ with ideal input states $\{\rho_i^{\text{ideal}}\}$. Similarly, we can get a process matrix of SPAM $\chi_{\text{exp}}^{\text{SPAM}}$ whose corresponding theoretical matrix χ^{I} is equal to the perfect identity operation with only one nonzero element $\chi_{\text{II,II}}^{\text{I}} = 1$. Therefore, the SPAM error is calculated as $1 - \text{Tr}(\chi_{\text{exp}}^{\text{SPAM}}\chi^{\text{I}}) = 0.3\%$. To facilitate error analysis, we then take another representation, the error matrix χ^{err} by factoring out the desired unitary operation, $U = U_{\text{CZ}}$ in this paper, from the standard process matrix χ_{exp}. We extract χ^{err} from the standard χ_{exp} matrix with the relations:

$$\chi^{\text{err}} = T\chi_{\text{exp}}T^\dagger, \quad T_{\text{mn}} = \text{Tr}(E_m^\dagger E_n U^\dagger)/d, \tag{F1}$$

where $U = U_{\text{CZ}}$, $d = 2^2$ for two-qubit CZ gate. In the ideal case, the error matrix is equal to χ^{I}; otherwise, the only one large element $\chi^{\mathrm{err}}_{\mathrm{II,II}}$ reflects the process fidelity $F_p = \mathrm{Tr}(\chi_{\mathrm{exp}}\chi_{\mathrm{ideal}}) = \mathrm{Tr}(\chi^{\mathrm{err}}\chi^{\mathrm{I}})$ and other nonzero elements indicate the imperfections of the gate. The imaginary parts of the elements along the left column and top row correspond to unitary imperfections, while the real parts of the elements come from decoherence error. We extract the infidelity induced by the dynamic ZZ coupling with $\epsilon_{ZZ} = (\mathrm{Im}(\chi^{\mathrm{err}}_{\mathrm{II},ZZ}))^2/F_p = 1.3\%$. And the decoherence error is assessed by

$$\epsilon_{\mathrm{dec}} = t_G\left(\frac{1}{2T_1^A} + \frac{1}{2T_1^B} + \frac{1}{2T_\varphi^A} + \frac{1}{2T_\varphi^B}\right) = 4.3\%, \qquad \text{(F2)}$$

where t_G is the gate duration, T_1 is the energy relaxation time, T_φ is the pure dephasing time, and the qubits are labeled as A and B.

APPENDIX G: ROBUSTNESS OF SP NGQC GATES

To explain the noise-resilient features of different types of gates [86,87], we add a Rabi frequency error term $\epsilon = \delta A/A$ satisfying $|\epsilon| \ll 1$ into the Hamiltonian in Eq. (1) in the main text as follows:

$$H = \frac{1}{2}\begin{pmatrix} \Delta(t) & (1+\epsilon)\Omega_0\, e^{-i\varphi} \\ (1+\epsilon)\Omega_0\, e^{i\varphi} & -\Delta(t) \end{pmatrix}. \qquad \text{(G1)}$$

Here, we fix the Rabi frequency to Ω_0 because when we calculate the fidelity, we care about the integration of the Hamiltonian instead of the Hamiltonian itself. An example of fidelity difference between the time-dependent Rabi frequency and time-independent Rabi frequency is shown in Fig. 8, where $\Omega(t)_{\max} = \Omega_0$. The process fidelities differ by a factor of two because the total power of cosine envelope we use is half that of the time independent one by integration. So we can utilize the constant Rabi frequency by setting it to half of the maximum $\Omega(t)$.

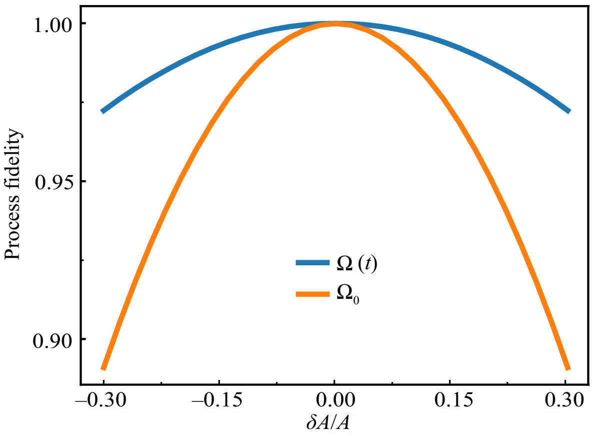

FIG. 8. Process fidelity of SP NGQC H gate against Rabi frequency error $\delta A/A$. Ω_0 is equal to the $\Omega(t)_{\max}$. The difference between process fidelities is 2 times.

The fidelity used to characterize the performance is defined as

$$F = \frac{|\mathrm{Tr}(U^\dagger_{\mathrm{ideal}}U)|}{\mathrm{Tr}(U^\dagger_{\mathrm{ideal}}U_{\mathrm{ideal}})}, \qquad \text{(G2)}$$

where U_{ideal} is the ideal gate operator and U is calculated through the Hamiltonian in Eq. (G1). We note that in the case of unitary evolution, the fidelity in Eq. (G2) is the square root of the process fidelity defined with χ matrix ($F_p = \mathrm{Tr}(\chi_{\mathrm{exp}}\chi_{\mathrm{ideal}})$). Then we get the process fidelity of the SP NGQC as $F_{\mathrm{SP\ NGQC}} = [1 + \cos\gamma - (\cos\gamma - 1)\cos(\epsilon\theta)]/2$ where only up to the second order of error ϵ is considered. Similarly, the process fidelities of NGQC and Dyn can be expressed as $F_{\mathrm{NGQC}} = 1 - \{(\pi^2/4)[1 - \cos(\gamma/2)] - [\theta(\pi-\theta)/2]\sin^2(\gamma/2)\}\epsilon^2$, $F_{\mathrm{Dyn}} = \cos(\gamma\epsilon/2)$ for X and Y gates and $F_{\mathrm{Dyn}} = |(\sin\pi\epsilon)/[4\sin(\pi\epsilon/4)]|$ for H gate, respectively. The calculated fidelities are overlaid on Figs. 3(a) and 3(b) in the main text, which shows our theoretical formulas agree well with the experimental results.

In the main text Fig. 3(e), we compare the performance of SP NGQC and NGQC scheme over the full single-qubit gate space against Rabi frequency error. Here, we also compare the performance of SP NGQC and dynamical scheme for some special gates, shown in Fig. 9(a). The dynamical rotation of any rotation axis can be decomposed into Y-X-Y composite pulse sequence and its process fidelity is affected by three parameters, θ, φ for rotation axis and γ for rotation angle. Here we choose $\varphi = 0$ for an example to show the superior robustness of the SP NGQC scheme against Rabi frequency error than the dynamical scheme. For the sake of completeness, the error robustness of Z rotations against the Rabi frequency error and frequency shift error are shown in Figs. 9(b) and 9(c).

In the main text, we also investigate the influence of frequency detuning error $\delta\Delta$ to the fidelities of single-qubit SP NGQC gates, NGQC gates, and dynamical gates. We numerically simulate the system by adding a qubit frequency shift error term to the Hamiltonian:

$$H = \frac{1}{2}\begin{pmatrix} \Delta(t) + \delta\Delta & \Omega_0\, e^{-i\varphi} \\ \Omega_0\, e^{i\varphi} & -\Delta(t) - \delta\Delta \end{pmatrix} \qquad \text{(G3)}$$

and the results match well in Figs. 3(c) and 3(d). Considering the frequency shift error, dynamical gates work better because the frequency shifts strongly affect the global change of the evolution path, especially the intervals in Eq. (2b) of the SP NGQC scheme, thus giving a limitation to the SP NGQC scheme. In experimental conditions, the frequency can be accurately manipulated in our superconducting system with fluctuations at kHz level. In practical experiments, one can choose an appropriate scheme against the dominant error in the system.

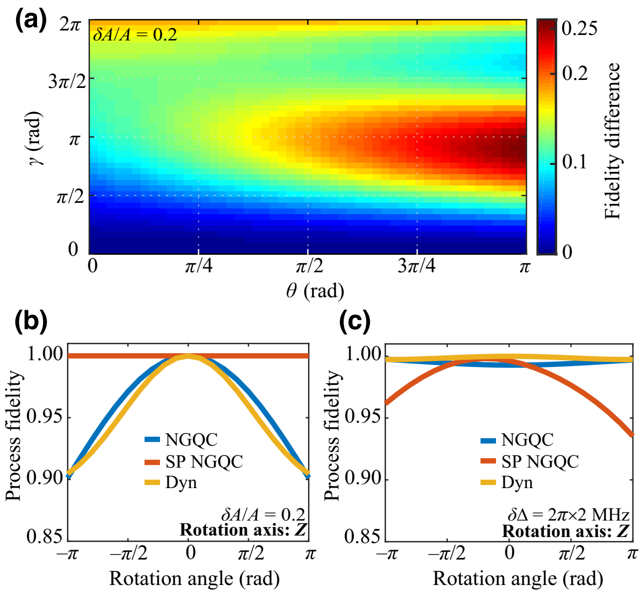

FIG. 9. (a) The landscape of process fidelity difference $F_{\text{SP NGQC}} - F_{\text{Dyn}}$ against Rabi frequency error, where $\delta A/A = 0.2$. The azimuth angle φ is 0 when the rotation axis is in the X-Z plane. The dynamical gates are realized by composite Y-X-Y sequences. $\theta = 0$ corresponds to the Z rotation and $\theta = \pi/2$ is X rotation. The SP NGQC scheme performs much better than the dynamical scheme. (b) The performance of three schemes' Z rotation against Rabi frequency error, where $\delta A/A = 0.2$. (c) The performance of three schemes' Z rotation against frequency shift error, where $\delta\Delta = 2\pi \times 2$ MHz.

APPENDIX H: RANDOMIZED BENCHMARKING

We also use another conventional method, Clifford-based randomized benchmarking to characterize the nonadiabatic geometric quantum gates [70–72]. In the single-qubit reference RB experiment, the state is prepared in $|0\rangle$ and follows a series of randomly chosen Clifford gates from the single-qubit Clifford group. Finally, a reverse gate is applied to bring the qubit back to $|0\rangle$. We measure the survival probability of state $|0\rangle$ (the sequence fidelity) as the number of single-qubit Clifford gates m increases. The whole experiment is repeated for $k = 30$ different sequences to get the average sequence fidelity. The maximum number of Clifford gates is restricted by the measuring instrument with at most 30-μs driving time. In the interleaved RB experiment, we insert a specific gate G after each randomly chosen Clifford gate and a similar reverse gate is applied to invert the whole sequence. The transformation of gate errors to a depolarizing channel leads to an exponential decay of the ground-state population towards the maximally mixed state, where the decay rate is a measure of the average gate fidelity. Therefore, we fit both reference and interleaved sequence fidelity curves to $F = Ap^m + B$ with different decay rates p_{ref} and p_{int}. SPAM errors are absorbed in parameters A and B and thus do not affect the extracted fidelities. The average gate fidelity is given by $F_{\text{ref}} = 1 - (1 - p_{\text{ref}})(d-1)/d$ where $d = 2^N$ for N qubits. The specific fidelity for gate G can be calculated by $F_{\text{gate}} = 1 - (1 - p_{\text{int}}/p_{\text{ref}})(d-1)/d$.

For two-qubit Clifford-based RB, the experiment is similar, but with the randomly chosen Clifford gates from the two-qubit Clifford group instead. We cannot simply estimate the two-qubit gate error per Clifford gates through the reference RB because two-qubit Clifford gates contain both single- and two-qubit gates. Also, we get the specific fidelity by interleaved RB and $F_{\text{gate}} = 1 - (1 - p_{\text{int}}/p_{\text{ref}})(d-1)/d$.

1. Leakage RB

We estimate the average leakage error of our short-path nonadiabatic geometric CZ gate from the reference and interleaved RB experiment by fitting the population in the computational subspace $P_{\chi 1} \equiv P_{00} + P_{01} + P_{10} + P_{11}$ [77,78], instead of the P_{00}, to an exponential model:

$$P_{\chi 1,\text{ref}} = A_{\text{ref}} + B_{\text{ref}}(\lambda_{1,\text{ref}})^m, \tag{H1}$$

$$P_{\chi 1,\text{int}} = A_{\text{int}} + B_{\text{int}}(\lambda_{1,\text{int}})^m. \tag{H2}$$

Then, we calculate the average leakage rates L_{ref} and L_{int} per Clifford gate as follows:

$$L_{1,\text{ref}} = (1 - A_{\text{ref}})(1 - \lambda_{1,\text{ref}}), \tag{H3}$$

$$L_{1,\text{int}} = (1 - A_{\text{int}})(1 - \lambda_{1,\text{int}}). \tag{H4}$$

The average leakage rate per CZ gate is subsequently obtained by

$$L_1^{\text{CZ}} = 1 - \frac{1 - L_{1,\text{int}}}{1 - L_{1,\text{ref}}}. \tag{H5}$$

The leakage rate L_{CZ} per CZ gate is extracted as 0.13%. Analyzing the residual state populations, we find that most leakage probabilities are lying on the $|20\rangle$, which indicates it may come from the residual pulse distortion in Z-control pulses of Q_A.

2. Purity RB

We utilize purity RB to distinguish between coherent errors due to mistakes in our calibration, versus incoherent error due to noise in the qubit's environment [79]. The experiment is done by performing QST to determine the state of the qubit after the random sequence, instead of just measuring the state probabilities. The purity of the state is defined as $P = \text{tr}(\rho^2)$. Starting in the ground state, the purity satisfies

$$P = \left(1 - \frac{1}{d}\right)\gamma^{2m} + \frac{1}{d} \tag{H6}$$

after m Clifford gates with a pure depolarizing noise γ. Accordingly, we fit the data to $A\gamma^{2m} + B$ and the incoherent error per CZ gate is estimated as $\epsilon = \frac{3}{4}(1 - \gamma^{2/3}) =$ 3.7%. This value is comparable with the results obtained from QPT, demonstrating that our gate is dominated by incoherent errors.

APPENDIX I: TWO-QUBIT SP NGQC CZ GATE

We use the parametric driving method to change the coupling strength between the two qubits. For the first interval, we choose $\nu,\ \varepsilon$ to satisfy the resonance condition $|\bar{\omega}_A - \omega_B| - \alpha_A = 2\nu$, the Hamiltonian in the subspace can be written as

$$H = \frac{1}{2}\begin{pmatrix} 0 & g_{\mathrm{eff}}\, e^{i\beta} \\ g_{\mathrm{eff}}\, e^{-i\beta} & 0 \end{pmatrix} \tag{I1}$$

under the rotation frame, where $\beta = \Phi + \pi/2$. And the rotation frame is selected. Once we change the parametric modulation to $\omega'_A(t) = \bar{\omega}'_A + \varepsilon' \cos(2\nu' t + 2\beta')$ in the second segment, the Hamiltonian in the same rotating frame turns into

$$H = \frac{1}{2}\begin{pmatrix} H_{11} & g_{\mathrm{eff}}\, e^{i\beta} \\ g_{\mathrm{eff}}\, e^{-i\beta} & H_{20} \end{pmatrix}, \tag{I2}$$

$$\begin{aligned} H_{11} &= \omega_A(t) - \omega'_A(t) \\ &= \varepsilon' - \varepsilon + \varepsilon' \cos(2\nu' t + 2\beta') - \varepsilon \cos(2\nu t + 2\beta), \end{aligned} \tag{I3}$$

$$H_{20} = -H_{11}. \tag{I4}$$

In the experiment, we choose ν' and β' to remain constant and change the modulation amplitude ε. And the third interval's Hamiltonian is the same as the first one. The final evolution trajectory is shown in Fig. 10(a). The trajectory approximately forms a hemisphere with subtle oscillation, which comes from H_{11} and H_{20}. The greater the modulation amplitude ε' differs from ε, the corresponding $\Delta'/2\pi$ is also larger, which will lead to more severe oscillation and destroy the geometric phase.

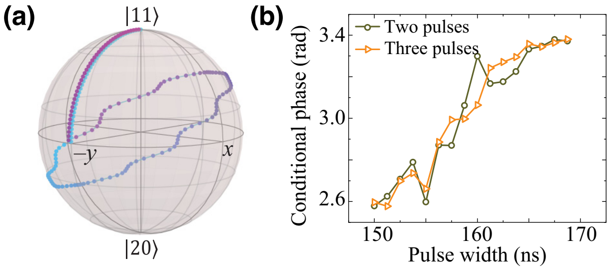

FIG. 10. (a) The evolution trajectory of our CZ gate in the $|11\rangle - |20\rangle$ space. The evolutionary time sequence is marked by the dots' color from light blue to dark violet. (b) Conditional phase of the CPHASE gate versus the second segment's pulse width with (without) the final half-π pulse. The final half-π pulse does not influence the conditional phase through geodesic principle.

As shown in Fig. 10(b), the conditional phase acquired by the pulse sequence shown in Fig. 4(a) with (without) the final half-π pulse remains nearly the same because the final segment is moving along the geodesic to bring the state back to $|11\rangle$, which does not change the final geometric phase.

APPENDIX J: AN ALTERNATIVE SOLUTION FOR TWO-QUBIT SP NGQC CZ GATE

We theoretically present another solution for the two-qubit short-path geometric CZ gate that regards the three intervals of the CZ gate as a whole one. Considering a typical parametric modulation function $F(t) = A(t)\sin[(\omega_B - \omega_A + \delta(t) + \alpha_A)t + \beta(t)]$, where $A(t)$, $\delta(t)$, and $\beta(t)$ indicate the strength, frequency detuning, and phase of the modulated field, respectively, the frequency of Q_A is modulated as $\omega_A(t) = \omega_A + \dot{F}(t)$. Unitary transformation $U = U_1 \times U_2$ is carried out with

$$U_1 = \exp\left[i\begin{pmatrix} 0 & & \\ & \omega_A & \\ & & 2\omega_A - \alpha_A \end{pmatrix} \otimes \begin{pmatrix} 1 & & \\ & 1 & \\ & & 1 \end{pmatrix} t + i\begin{pmatrix} 1 & & \\ & 1 & \\ & & 1 \end{pmatrix} \otimes \begin{pmatrix} 0 & & \\ & \omega_B & \\ & & 2\omega_B - \alpha_B \end{pmatrix} t\right], \tag{J1}$$

$$U_2 = \exp\left[i\begin{pmatrix} 0 & & \\ & F(t) & \\ & & 2F(t) \end{pmatrix} \otimes \begin{pmatrix} 1 & & \\ & 1 & \\ & & 1 \end{pmatrix} t\right]. \tag{J2}$$

After the unitary transformation and utilizing Jacobi-Anger expansion, we can get an effective Hamiltonian

$$H = \sqrt{2} g_{AB} J_1[A(t)] \begin{pmatrix} 0 & e^{-i[\delta(t)t+\beta(t)]} \\ e^{i[\delta(t)t+\beta(t)]} & 0 \end{pmatrix} \tag{J3}$$

in the subspace $\{|11\rangle, |20\rangle\}$ by applying the rotating-wave approximation, which ignores the high-frequency oscillation terms. Here $J_1[A(t)]$ is the first-order Bessel function of the first kind. Now we apply a second unitary transformation by $U_3 = \exp[-i\delta(t)t\sigma_z/2]$. In this frame, the Hamiltonian can be rewritten as

$$H = \frac{1}{2} \begin{pmatrix} \dot{\delta}(t)t + \delta(t) & g e^{-i\beta(t)} \\ g e^{i\beta(t)} & -\dot{\delta}(t)t - \delta(t) \end{pmatrix}, \tag{J4}$$

where $g = 2\sqrt{2} g_{AB} J_1[A(t)]$ is the effective coupling strength between the two qubits. This Hamiltonian is the same as Eq. (1). By adjusting $\delta(t)$, $A(t)$, and $\beta(t)$ to follow the cyclic evolution conditions shown in Eq. (2), we can realize the geometric phase gate

$$\begin{pmatrix} \exp\left(-\frac{i\gamma'}{2}\right) & 0 \\ 0 & \exp\left(\frac{i\gamma'}{2}\right) \end{pmatrix}$$

in the subspace $\{|11\rangle, |20\rangle\}$. Setting $\gamma' = 2\pi$, it is a CZ gate in the two-qubit computational space. The actual flux pulse applied to the Z control line is calculated by

$$V(t) = f^{-1}[\dot{F}(t)], \tag{J5}$$

where f is the nonlinear frequency response of the transmon qubit.

As an example, we utilize the flat-top Gaussian shape to smoothly change the $\delta(t)$, $A(t)$, and $\beta(t)$ to guarantee the existence of the derivative of $F(t)$. To satisfy the conditions for nonadiabatic geometric CZ gate, we constrain the parameters to

$$\dot{\delta}(t)t + \delta(t) = \frac{\Delta_0}{2}\left[\operatorname{erf}\left(\frac{t-t_b}{\sqrt{2}\sigma}\right) - \operatorname{erf}\left(\frac{t-t_b-t_c}{\sqrt{2}\sigma}\right)\right], \tag{J6a}$$

$$A(t) = A_0 - \frac{A_0}{2}\left[\operatorname{erf}\left(\frac{t-t_b-t_c}{\sqrt{2}\sigma}\right) - \operatorname{erf}\left(\frac{t-t_b}{\sqrt{2}\sigma}\right)\right] + \text{offset}, \tag{J6b}$$

$$\beta(t) = \begin{cases} 0 \\ \frac{\pi}{2}\left[\operatorname{erf}\left(\frac{t-t_{b1}}{\sqrt{2}\sigma}\right) - \operatorname{erf}\left(\frac{t-t_{b1}-t_{c1}}{\sqrt{2}\sigma}\right)\right], \\ 0 \end{cases} \tag{J6c}$$

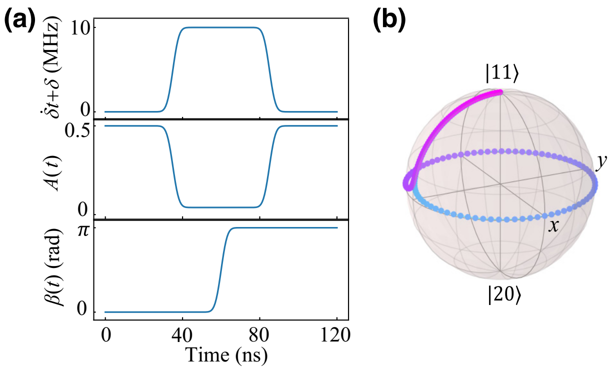

FIG. 11. (a) An example of pulse parameters based on Eq. (J6). Δ_0 is chosen to be $2\pi \times 10$ MHz. A_0 and offset make the *on-off* ratio of the effective coupling strength to be 10, large enough for a pure Z rotation. β is changed between 0 and π to make the state back to $|11\rangle$. (b) Evolution of the $|11\rangle$ according to the pulse parameters shown in (a).The evolutionary time sequence is marked by the dots' color from light blue to dark violet.

where t_b is the rotation time around x-y axes in the $\{|11\rangle, |20\rangle\}$ subspace which is controlled by A_0, t_c is the rotation time around z axis, which is controlled by Δ, t_{b1}, and t_{c1} are chosen to make the phase transition happen in the time interval of z rotation, and σ determines the ramping rate of the parameters. A little offset is added to $A(t)$ to ensure that the pulse amplitude is nonzero and g is small compared to Δ. The pulse and the evolution trajectory are shown in Fig. 11 [88,89].

In principle, this solution can reach a fidelity higher than 99% with shorter gate time than the CZ gate described in the main text. However, this solution works at a flux bias far from the sweet spot where the qubit suffers more from the $1/f$ noise. Also, the solution changes the parametric modulation frequency during the evolution, which requires a real-time crosstalk correction. To acquire an ideal value of γ', it requires adjusting $\delta(t)$, $A(t)$, and $\beta(t)$ with multiple parameters simultaneously, indicating a quite complicated control optimization scheme, which is more susceptible to control errors, thus we do not show it experimentally in the main text.

[1] J. Preskill, Quantum computing in the NISQ era and beyond, Quantum **2**, 79 (2018).

[2] P. Shor, in *Proceedings of 37th Conference on Foundations of Computer Science* (IEEE, Burlington, 1996), pp. 56–65.

[3] R. Raussendorf and J. Harrington, Fault-Tolerant Quantum Computation with High Threshold in Two Dimensions, Phys. Rev. Lett. **98**, 190504 (2007).

[4] A. G. Fowler, M. Mariantoni, J. M. Martinis, and A. N. Cleland, Surface codes: Towards practical large-scale quantum computation, Phys. Rev. A **86**, 032324 (2012).

[5] S. Lloyd, Almost any Quantum Logic Gate is Universal, Phys. Rev. Lett. **75**, 346 (1995).

[6] M. J. Bremner, C. M. Dawson, J. L. Dodd, A. Gilchrist, A. W. Harrow, D. Mortimer, M. A. Nielsen, and T. J. Osborne, Practical Scheme for Quantum Computation with Any Two-Qubit Entangling Gate, Phys. Rev. Lett. **89**, 247902 (2002).

[7] M. V. Berry, Quantal phase factors accompanying adiabatic changes, Proc. R. Soc. Lond. A Math. Phys. Sci. **392**, 45 (1984).

[8] F. Wilczek and A. Zee, Appearance of Gauge Structure in Simple Dynamical Systems, Phys. Rev. Lett. **52**, 2111 (1984).

[9] Y. Aharonov and J. Anandan, Phase Change During a Cyclic Quantum Evolution, Phys. Rev. Lett. **58**, 1593 (1987).

[10] J. Anandan, Non-adiabatic non-Abelian geometric phase, Phys. Lett. A **133**, 171 (1988).

[11] G. De Chiara, G. M. Palma, Berry Phase for a Spin 1/2 Particle in a Classical Fluctuating Field, Phys. Rev. Lett. **91**, 090404 (2003).

[12] A. Carollo, I. Fuentes-Guridi, M. F. M. C. Santos, and V. Vedral, Spin-1/2 Geometric Phase Driven by Decohering Quantum Fields, Phys. Rev. Lett. **92**, 020402 (2004).

[13] S.-L. Zhu and P. Zanardi, Geometric quantum gates that are robust against stochastic control errors, Phys. Rev. A **72**, 020301 (2005).

[14] P. J. Leek, J. M. Fink, A. Blais, R. Bianchetti, M. Göppl, J. M. Gambetta, D. I. Schuster, L. Frunzio, R. J. Schoelkopf, and A. Wallraff, Observation of Berry's phase in a solid-state qubit, Science **318**, 1889 (2007).

[15] S. Filipp, J. Klepp, Y. Hasegawa, C. Plonka-Spehr, U. Schmidt, P. Geltenbort, and H. Rauch, Experimental Demonstration of the Stability of Berry's Phase for a Spin-1/2 Particle, Phys. Rev. Lett. **102**, 030404 (2009).

[16] J. T. Thomas, M. Lababidi, and M. Tian, Robustness of single-qubit geometric gate against systematic error, Phys. Rev. A **84**, 042335 (2011).

[17] M. Johansson, E. Sjöqvist, L. M. Andersson, M. Ericsson, B. Hessmo, K. Singh, and D. M. Tong, Robustness of nonadiabatic holonomic gates, Phys. Rev. A **86**, 062322 (2012).

[18] S. Berger, M. Pechal, A. A. Abdumalikov, C. Eichler, L. Steffen, A. Fedorov, A. Wallraff, and S. Filipp, Exploring the effect of noise on the Berry phase, Phys. Rev. A **87**, 060303 (2013).

[19] H. Wu, E. M. Gauger, R. E. George, M. Möttönen, H. Riemann, N. V. Abrosimov, P. Becker, H.-J. Pohl, K. M. Itoh, M. L. W. Thewalt, and J. J. L. Morton, Geometric phase gates with adiabatic control in electron spin resonance, Phys. Rev. A **87**, 032326 (2013).

[20] Y.-Y. Huang, Y.-K. Wu, F. Wang, P.-Y. Hou, W.-B. Wang, W.-G. Zhang, W.-Q. Lian, Y.-Q. Liu, H.-Y. Wang, H.-Y. Zhang, L. He, X.-Y. Chang, Y. Xu, and L.-M. Duan, Experimental Realization of Robust Geometric Quantum Gates with Solid-State Spins, Phys. Rev. Lett. **122**, 010503 (2019).

[21] P. Zanardi and M. Rasetti, Holonomic quantum computation, Phys. Lett. A **264**, 94 (1999).

[22] J. A. Jones, V. Vedral, A. Ekert, and G. Castagnoli, Geometric quantum computation using nuclear magnetic resonance, Nature **403**, 869 (2000).

[23] L.-M. Duan, J. I. Cirac, and P. Zoller, Geometric manipulation of trapped ions for quantum computation, Science **292**, 1695 (2001).

[24] L.-A. Wu, P. Zanardi, and D. A. Lidar, Holonomic Quantum Computation in Decoherence-Free Subspaces, Phys. Rev. Lett. **95**, 130501 (2005).

[25] K. Toyoda, K. Uchida, A. Noguchi, S. Haze, and S. Urabe, Realization of holonomic single-qubit operations, Phys. Rev. A **87**, 052307 (2013).

[26] F. Leroux, K. Pandey, R. Rehbi, F. Chevy, C. Miniatura, B. Grémaud, and D. Wilkowski, Non-Abelian adiabatic geometric transformations in a cold strontium gas, Nat. Commun. **9**, 3580 (2018).

[27] M. G. Bason, M. Viteau, N. Malossi, P. Huillery, E. Arimondo, D. Ciampini, R. Fazio, V. Giovannetti, R. Mannella, and O. Morsch, High-fidelity quantum driving, Nat. Phys. **8**, 147 (2012).

[28] X.-K. Song, H. Zhang, Q. Ai, J. Qiu, and F.-G. Deng, Shortcuts to adiabatic holonomic quantum computation in decoherence-free subspace with transitionless quantum driving algorithm, New J. Phys. **18**, 023001 (2016).

[29] J. Zhang, T. H. Kyaw, D. Tong, E. Sjöqvist, and L.-C. Kwek, Fast non-Abelian geometric gates via transitionless quantum driving, Sci. Rep. **5**, 1 (2016).

[30] B. B. Zhou, A. Baksic, H. Ribeiro, C. G. Yale, F. J. Heremans, P. C. Jerger, A. Auer, G. Burkard, A. A. Clerk, and D. D. Awschalom, Accelerated quantum control using superadiabatic dynamics in a solid-state lambda system, Nat. Phys. **13**, 330 (2017).

[31] F. Kleißler, A. Lazariev, and S. Arroyo-Camejo, Universal, high-fidelity quantum gates based on superadiabatic, geometric phases on a solid-state spin-qubit at room temperature, npj Quantum Inf. **4**, 1 (2018).

[32] T. Yan, B.-J. Liu, K. Xu, C. Song, S. Liu, Z. Zhang, H. Deng, Z. Yan, H. Rong, K. Huang, M.-H. Yung, Y. Chen, and D. Yu, Experimental Realization of Nonadiabatic Shortcut to Non-Abelian Geometric Gates, Phys. Rev. Lett. **122**, 080501 (2019).

[33] J. Chu, D. Li, X. Yang, S. Song, Z. Han, Z. Yang, Y. Dong, W. Zheng, Z. Wang, X. Yu, D. Lan, X. Tan, and Y. Yu, Realization of Superadiabatic Two-Qubit Gates using Parametric Modulation in Superconducting Circuits, Phys. Rev. Appl. **13**, 064012 (2020).

[34] L. Qiu, H. Li, Z. Han, W. Zheng, X. Yang, Y. Dong, S. Song, D. Lan, X. Tan, and Y. Yu, Experimental realization of noncyclic geometric gates with shortcut to adiabaticity in a superconducting circuit, Appl. Phys. Lett. **118**, 254002 (2021).

[35] B.-J. Liu, X.-K. Song, Z.-Y. Xue, X. Wang, and M.-H. Yung, Plug-and-Play Approach to Nonadiabatic Geometric Quantum Gates, Phys. Rev. Lett. **123**, 100501 (2019).

[36] T. Chen, P. Shen, and Z.-Y. Xue, Robust and Fast Holonomic Quantum Gates with Encoding on Superconducting Circuits, Phys. Rev. Appl. **14**, 034038 (2020).

[37] A. A. Abdumalikov, Jr., J. M. Fink, K. Juliusson, M. Pechal, S. Berger, A. Wallraff, and S. Filipp, Experimental

realization of non-Abelian non-adiabatic geometric gates, Nature **496**, 482 (2013).

[38] Y. Xu, W. Cai, Y. Ma, X. Mu, L. Hu, T. Chen, H. Wang, Y. P. Song, Z.-Y. Xue, Z.-Q. Yin, and L. Sun, Single-Loop Realization of Arbitrary Nonadiabatic Holonomic Single-Qubit Quantum Gates in a Superconducting Circuit, Phys. Rev. Lett. **121**, 110501 (2018).

[39] Z. Zhang, P. Z. Zhao, T. Wang, L. Xiang, Z. Jia, P. Duan, D. M. Tong, Y. Yin, and G. Guo, Single-shot realization of nonadiabatic holonomic gates with a superconducting Xmon qutrit, New J. Phys. **21**, 073024 (2019).

[40] S. Li, B.-J. Liu, Z. Ni, L. Zhang, Z.-Y. Xue, J. Li, F. Yan, Y. Chen, S. Liu, M.-H. Yung, Y. Xu, and D. Yu, Superrobust Geometric Control of a Superconducting Circuit, Phys. Rev. Appl. **16**, 064003 (2021).

[41] G. Feng, G. Xu, and G. Long, Experimental Realization of Nonadiabatic Holonomic Quantum Computation, Phys. Rev. Lett. **110**, 190501 (2013).

[42] C. Zu, W.-B. Wang, L. He, W.-G. Zhang, C.-Y. Dai, F. Wang, and L.-M. Duan, Experimental realization of universal geometric quantum gates with solid-state spins, Nature **514**, 72 (2014).

[43] S. Arroyo-Camejo, A. Lazariev, S. W. Hell, and G. Balasubramanian, Room temperature high-fidelity holonomic single-qubit gate on a solid-state spin, Nat. Commun. **5**, 4870 (2014).

[44] C. Song, S.-B. Zheng, P. Zhang, K. Xu, L. Zhang, Q. Guo, W. Liu, D. Xu, H. Deng, K. Huang *et al.*, Continuous-variable geometric phase and its manipulation for quantum computation in a superconducting circuit, Nat. Commun. **8**, 1061 (2017).

[45] Y. Sekiguchi, N. Niikura, R. Kuroiwa, H. Kano, and H. Kosaka, Optical holonomic single quantum gates with a geometric spin under a zero field, Nat. Photonics **11**, 309 (2017).

[46] B. B. Zhou, P. C. Jerger, V. O. Shkolnikov, F. J. Heremans, G. Burkard, and D. D. Awschalom, Holonomic Quantum Control by Coherent Optical Excitation in Diamond, Phys. Rev. Lett. **119**, 140503 (2017).

[47] K. Nagata, K. Kuramitani, Y. Sekiguchi, and H. Kosaka, Universal holonomic quantum gates over geometric spin qubits with polarised microwaves, Nat. Commun. **9**, 3227 (2018).

[48] N. Ishida, T. Nakamura, T. Tanaka, S. Mishima, H. Kano, R. Kuroiwa, Y. Sekiguchi, and H. Kosaka, Universal holonomic single quantum gates over a geometric spin with phase-modulated polarized light, Opt. Lett. **43**, 2380 (2018).

[49] D. Egger, M. Ganzhorn, G. Salis, A. Fuhrer, P. Müller, P. Barkoutsos, N. Moll, I. Tavernelli, and S. Filipp, Entanglement Generation in Superconducting Qubits using Holonomic Operations, Phys. Rev. Appl. **11**, 014017 (2019).

[50] M.-Z. Ai, S. Li, Z. Hou, R. He, Z.-H. Qian, Z.-Y. Xue, J.-M. Cui, Y.-F. Huang, C.-F. Li, and G.-C. Guo, Experimental Realization of Nonadiabatic Holonomic Single-Qubit Quantum Gates with Optimal Control in a Trapped Ion, Phys. Rev. Appl. **14**, 054062 (2020).

[51] D. Leibfried, B. DeMarco, V. Meyer, D. Lucas, M. Barrett, J. Britton, W. M. Itano, B. Jelenković, C. Langer, T. Rosenband *et al.*, Experimental demonstration of a robust, high-fidelity geometric two ion-qubit phase gate, Nature **422**, 412 (2003).

[52] Y. Xu, Z. Hua, T. Chen, X. Pan, X. Li, J. Han, W. Cai, Y. Ma, H. Wang, Y. P. Song, Z.-Y. Xue, and L. Sun, Experimental Implementation of Universal Nonadiabatic Geometric Quantum Gates in a Superconducting Circuit, Phys. Rev. Lett. **124**, 230503 (2020).

[53] P. Zhao, Z. Dong, Z. Zhang, G. Guo, D. Tong, and Y. Yin, Experimental realization of nonadiabatic geometric gates with a superconducting Xmon qubit, Sci. China Phys. Mech. Astron. **64**, 250362 (2021).

[54] J. Koch, T. M. Yu, J. Gambetta, A. A. Houck, D. I. Schuster, J. Majer, A. Blais, M. H. Devoret, S. M. Girvin, and R. J. Schoelkopf, Charge-insensitive qubit design derived from the cooper pair box, Phys. Rev. A **76**, 042319 (2007).

[55] R. Barends, J. Kelly, A. Megrant, A. Veitia, D. Sank, E. Jeffrey, T. C. White, J. Mutus, A. G. Fowler, B. Campbell *et al.*, Superconducting quantum circuits at the surface code threshold for fault tolerance, Nature **508**, 500 (2014).

[56] B.-J. Liu, S.-L. Su, and M.-H. Yung, Nonadiabatic noncyclic geometric quantum computation in Rydberg atoms, Phys. Rev. Res. **2**, 043130 (2020).

[57] T. Chen and Z.-Y. Xue, High-Fidelity and Robust Geometric Quantum Gates that Outperform Dynamical Ones, Phys. Rev. Appl. **14**, 064009 (2020).

[58] J. W. Zhang, L.-L. Yan, J. C. Li, G. Y. Ding, J. T. Bu, L. Chen, S.-L. Su, F. Zhou, and M. Feng, Single-Atom Verification of the Noise-Resilient and Fast Characteristics of Universal Nonadiabatic Noncyclic Geometric Quantum Gates, Phys. Rev. Lett. **127**, 030502 (2021).

[59] L.-N. Ji, C.-Y. Ding, T. Chen, and Z.-Y. Xue, Noncyclic geometric quantum gates with smooth paths via invariant-based shortcuts, Adv. Quantum Technol. **4**, 2100019 (2021).

[60] K. Z. Li, P. Z. Zhao, and D. M. Tong, Approach to realizing nonadiabatic geometric gates with prescribed evolution paths, Phys. Rev. Res. **2**, 023295 (2020).

[61] C.-Y. Ding, L.-N. Ji, T. Chen, and Z.-Y. Xue, Path-optimized nonadiabatic geometric quantum computation on superconducting qubits, Quantum Sci. Technol. **7**, 015012 (2021).

[62] C.-Y. Ding, Y. Liang, K.-Z. Yu, and Z.-Y. Xue, Nonadiabatic geometric quantum computation with shortened path on superconducting circuits, Appl. Phys. Lett. **119**, 184001 (2021).

[63] Y. Li, Y. Dong, W. Zheng, Y. Zhang, Z. Ma, Q. Liu, J. Wang, Y. Li, Y. Liu, J. Zhao, D. Lan, S. Li, X. Tan, and Y. Yu, Nonadiabatic geometric gates with a shortened loop in a superconducting circuit, Phys. Status Solidi (b) **259**, 2200040 (2022).

[64] S. Li, J. Xue, T. Chen, and Z.-Y. Xue, High-fidelity geometric quantum gates with short paths on superconducting circuits, Adv. Quantum Technol. **4**, 2000140 (2021).

[65] D. C. McKay, C. J. Wood, S. Sheldon, J. M. Chow, and J. M. Gambetta, Efficient z gates for quantum computing, Phys. Rev. A **96**, 022330 (2017).

[66] P. Duan, Z.-F. Chen, Q. Zhou, W.-C. Kong, H.-F. Zhang, and G.-P. Guo, Mitigating Crosstalk-Induced Qubit Readout Error with Shallow-Neural-Network Discrimination, Phys. Rev. Appl. **16**, 024063 (2021).

[67] F. Motzoi, J. M. Gambetta, P. Rebentrost, and F. K. Wilhelm, Simple Pulses for Elimination of Leakage in Weakly Nonlinear Qubits, Phys. Rev. Lett. **103**, 110501 (2009).

[68] I. L. Chuang and M. A. Nielsen, Prescription for experimental determination of the dynamics of a quantum black box, J. Mod. Opt. **44**, 2455 (1997).

[69] J. L. O'Brien, G. J. Pryde, A. Gilchrist, D. F. V. James, N. K. Langford, T. C. Ralph, and A. G. White, Quantum Process Tomography of a Controlled-Not Gate, Phys. Rev. Lett. **93**, 080502 (2004).

[70] J. M. Chow, J. M. Gambetta, L. Tornberg, J. Koch, L. S. Bishop, A. A. Houck, B. R. Johnson, L. Frunzio, S. M. Girvin, and R. J. Schoelkopf, Randomized Benchmarking and Process Tomography for Gate Errors in a Solid-State Qubit, Phys. Rev. Lett. **102**, 090502 (2009).

[71] E. Knill, D. Leibfried, R. Reichle, J. Britton, R. B. Blakestad, J. D. Jost, C. Langer, R. Ozeri, S. Seidelin, and D. J. Wineland, Randomized benchmarking of quantum gates, Phys. Rev. A **77**, 012307 (2008).

[72] E. Magesan, J. M. Gambetta, B. R. Johnson, C. A. Ryan, J. M. Chow, S. T. Merkel, M. P. da Silva, G. A. Keefe, M. B. Rothwell, T. A. Ohki, M. B. Ketchen, and M. Steffen, Efficient Measurement of Quantum Gate Error by Interleaved Randomized Benchmarking, Phys. Rev. Lett. **109**, 080505 (2012).

[73] N. Didier, E. A. Sete, M. P. da Silva, and C. Rigetti, Analytical modeling of parametrically modulated transmon qubits, Phys. Rev. A **97**, 022330 (2018).

[74] S. A. Caldwell *et al.*, Parametrically Activated Entangling Gates using Transmon Qubits, Phys. Rev. Appl. **10**, 034050 (2018).

[75] J. Samuel and R. Bhandari, General Setting for Berry's Phase, Phys. Rev. Lett. **60**, 2339 (1988).

[76] A. N. Korotkov, Error matrices in quantum process tomography, arXiv:1309.6405.

[77] C. J. Wood and J. M. Gambetta, Quantification and characterization of leakage errors, Phys. Rev. A **97**, 032306 (2018).

[78] Y. Sung, L. Ding, J. Braumüller, A. Vepsäläinen, B. Kannan, M. Kjaergaard, A. Greene, G. O. Samach, C. McNally, D. Kim, A. Melville, B. M. Niedzielski, M. E. Schwartz, J. L. Yoder, T. P. Orlando, S. Gustavsson, and W. D. Oliver, Realization of High-Fidelity CZ and ZZ-Free iSWAP Gates with a Tunable Coupler, Phys. Rev. X **11**, 021058 (2021).

[79] J. Wallman, C. Granade, R. Harper, and S. T. Flammia, Estimating the coherence of noise, New J. Phys. **17**, 113020 (2015).

[80] F. Yan, P. Krantz, Y. Sung, M. Kjaergaard, D. L. Campbell, T. P. Orlando, S. Gustavsson, and W. D. Oliver, Tunable Coupling Scheme for Implementing High-Fidelity Two-Qubit Gates, Phys. Rev. Appl. **10**, 054062 (2018).

[81] D. C. McKay, S. Filipp, A. Mezzacapo, E. Magesan, J. M. Chow, and J. M. Gambetta, Universal Gate for Fixed-Frequency Qubits via a Tunable Bus, Phys. Rev. Appl. **6**, 064007 (2016).

[82] C. D. Bruzewicz, J. Chiaverini, R. McConnell, and J. M. Sage, Trapped-ion quantum computing: Progress and challenges, Appl. Phys. Rev. **6**, 021314 (2019).

[83] X. Zhang, H.-O. Li, G. Cao, M. Xiao, G.-C. Guo, and G.-P. Guo, Semiconductor quantum computation, Natl. Sci. Rev. **6**, 32 (2018).

[84] Origin Quantum Inc., Quantum computer control system, https://qcloud.originqc.com.cn/en/product/chipEquipment/15.

[85] P. Duan, Z. Jia, C. Zhang, L. Du, H. Tao, X. Yang, L. Guo, Y. Chen, H. Zhang, Z. Peng, W. Kong, H.-O. Li, G. Cao, and G.-P. Guo, Broadband flux-pumped Josephson parametric amplifier with an on-chip coplanar waveguide impedance transformer, Appl. Phys. Express **14**, 042011 (2021).

[86] S.-B. Zheng, C.-P. Yang, and F. Nori, Comparison of the sensitivity to systematic errors between nonadiabatic non-Abelian geometric gates and their dynamical counterparts, Phys. Rev. A **93**, 032313 (2016).

[87] J. Jing, C.-H. Lam, and L.-A. Wu, Non-Abelian holonomic transformation in the presence of classical noise, Phys. Rev. A **95**, 012334 (2017).

[88] J. Johansson, P. Nation, and F. Nori, Qutip: An open-source python framework for the dynamics of open quantum systems, Comput. Phys. Commun. **183**, 1760 (2012).

[89] J. Johansson, P. Nation, and F. Nori, Qutip 2: A python framework for the dynamics of open quantum systems, Comput. Phys. Commun. **184**, 1234 (2013).